Science Advances
AAAS

advances.sciencemag.org/cgi/content/full/7/24/eabf6971/DC1

Supplementary Materials for

Sparse ab initio x-ray transmission spectrotomography for nanoscopic compositional analysis of functional materials

Zirui Gao*, Michal Odstrcil, Sebastian Böcklein, Dennis Palagin, Mirko Holler, Dario Ferreira Sanchez, Frank Krumeich, Andreas Menzel, Marco Stampanoni, Gerhard Mestl, Jeroen Anton van Bokhoven, Manuel Guizar-Sicairos*, Johannes Ihli*

*Corresponding author. Email: zirui.gao@psi.ch (Z.G.); manuel.guizar-sicairos@psi.ch (M.G.-S.); johannes.ihli@psi.ch (J.I.)

Published 9 June 2021, *Sci. Adv.* **7**, eabf6971 (2021)
DOI: 10.1126/sciadv.abf6971

The PDF file includes:

Extended Materials and Methods
Selective oxidation of *n*-butane to MA within an industrial setting
Suggested active sites in VPO catalysts
Ptychographic computed x-ray tomography and sensitivity to variations in incident energy
Local structure optimization
Figs. S1 to S15
Tables S1 and S2
Legends for movies S1 and S2
References

Other Supplementary Material for this manuscript includes the following:

(available at advances.sciencemag.org/cgi/content/full/7/24/eabf6971/DC1)

Movies S1 and S2

Extended Materials and Methods:

Spatial Resolution of XTNES Tomograms: The spatial resolution of the sparse-XTNES tomograms was estimated using Fourier shell correlation (FSC).(62) To do so we divided the full hyperspectral dataset in half and two independent spectro-tomograms were reconstructed. To estimate the spatial resolution of the entire hyperspectral tomogram we then calculated the correlation between these two tomograms in Fourier domain and estimated the resolution based on the intersection with a half-bit threshold. For both samples, we estimate a half-period spatial resolution of ~26 nm, Figure S4a, for the 4D hyperspectral tomogram. The full-period resolution is accordingly twice this value.

However, one must consider that the chemical information resides in changes of the spectra. These changes consequently have different signal-to-noise ratio than the whole signal, and therefore also different resolution. To estimate the spatial resolution of such changes in spectra we take from the two independently reconstructed hyperspectral tomograms, the coefficients $X_k(\mathbf{r})$, k=1,2,3,4 as defined in Eq. (1) in the main text and calculate the 3D FSC for each one of them. The half-period resolution results are shown in Figure S4b and S4c for the pristine and used catalyst, respectively, which provide upper and lower bounds for the spatial resolution of the different spectral modes. It should be noted that this does not directly correspond to the resolution of the different components (i)-(iv).

Kramers-Kronig transformation (KKT): KKT of voxel-level phase spectra were calculated based on a piecewise Laurent polynomial method, as described in Watts (2014) (40). Phase spectra, which were obtained from tomography reconstructions, were linearly interpolated between energies in the measured range, and extrapolated to the energy range from 0 to 500 keV using values at both edges of the spectra. Then for each energy point within the measured range, an absorption value of the transformed spectrum is calculated using analytical formulas derived from integration of the input phase spectrum over the whole energy range, these formulas are given in Eq. (10) and Table 1 in Watts (2014) (40).

Dose Estimation: The X-ray dose imparted to the specimens in a XTNES tomogram was estimated to be on the order of ~10^8 Gy. The estimated dose is based on the average area flux density of each ptychographic scan and the mass density of the specimen.(63) For this calculation the sample was assumed to consist entirely of vanadyl pyrophosphate.

Tomogram Analysis: Analysis, segmentation, and 3D rendering was carried out either using in-house developed Matlab routines or using Avizo. Prior to the analysis of the pristine XTNES tomogram we masked out the outermost 200 nm of the imaged cylinder, Figure S15. The masked region contained sample preparation artefacts in the form of FIB-milling implanted gallium and redeposited material.

Porosity Analysis: The catalyst pore-network was isolated by means of threshold segmentation of the structural/ electron density tomogram, followed by morphological operations to refine the segmentation. Pore size distributions (PSD), Figure S8, were calculated based on 3D thickness maps.(64) In consideration of the spatial-resolution estimates, apparent pores with a diameter smaller than 52 nm were excluded from size distributions. The connected pore volume was calculated based on neighborhood-based component labelling.

Interfacial Changes: To map the average change in density and chemical composition from the pore space across the interface into the bulk catalyst interior we calculated a series of 3D Euclidian maps up to 250 nm into the catalyst with an average step size of 25 nm. Maps were calculated using the binary mask defined in the pore analysis step.

Component Identification: Component identification was carried out via multivariate comparison. Compared were the voxel-level measured electron density, vanadium concentration and oxidation-state values with those of a table of reference components or materials. Material identification possibilities were as such limited to the considered components, provided in Table S1 are electron density, vanadium concentration and oxidation state values of potential materials previously reported to be found within or as part of VPO catalysts.(26, 28, 34, 35) Identification was based on the closest match between experimental and tabulated values. Provided in Figure S7 are 1D and 2D correlation histograms of the measured/ extracted values of the two catalyst samples. Added to these plots are markers of the identified components. In the presented case we largely refrained from a partial volume effect based analysis, i.e. the occupation of a single voxel by two or multiple materials, leading to voxel-level average electron density, vanadium concentration values and oxidation state weighted in accordance to the volumetric fractional occupancy of a voxel by the present materials. A combination of materials was only considered to account for the detection of V^{3+} in the pristine sample, explainable by a partial occupancy of $V(PO_3)_3$ and amorphous or nanocrystalline $(VO)_2P_2O_7$ (50/50). See also Figure S7.

General Material Characterization Methods

Catalyst Composition: The population average chemical composition of the industrial VPO catalysts was determined by inductively coupled plasma atomic emission spectrometry (ICP-AES). The catalyst was dissolved in aqueous H_2SO_4 prior to the measurement.

Bulk Vanadium Oxidation State: Following dissolution in aqueous H_2SO_4, the catalyst's average oxidation state was determined using redox titration. $KMnO_4$ and $FeSO_4$ were used as titration reagents to determine the amounts of V^{4+} and V^{5+} in the respective catalyst samples. The reported vanadium oxidation state in Table S2 represents the concentration average of both species.

Catalytic Properties and Performance: The performance of industrial VPO catalyst samples was evaluated over the whole catalyst lifetime using a 3-channel IR sensor (butane, CO, CO_2) after scrubbing all organic acids (maleic anhydride, acetic acid, acrylic acid) and drying of the reaction gas.

Porosity: Average pore size and total porosity of the pristine and used VPO catalyst, were determined on a bulk level by nitrogen physisorption and Mercury intrusion porosimetry. Prior to each measurement, the sample was degassed for 10 h. The pore diameters were calculated using the Washburn equation with a contact angle of 140°. The bulk- average results are given in Table S2.

Electron Microscopy (EM): Scanning electron micrographs (SEM) and energy-dispersive X-ray (EDX) spectroscopy maps were acquired using a Quanta 200F operated at 20 kV and equipped with an Octane Elect EDXS system. The as-obtained samples were deposited on a carbon tape supported on SEM stubs. Scanning transmission electron micrographs (STEM) and EDX maps were acquired using a Hitachi HD 2700CS; TEM

images on a FEI Talos microscope, both operated at 200 kV. For this, fractured samples were deposited on carbon coated cupper grids.

Powder-XRD: Powder-XRD measurements were performed using a Bruker D8 Advanced diffractometer equipped with a Cu X-ray source, Figure S12. Rietveld refinement was performed using Maud.(65)

Scanning X-ray Fluorescence and X-ray Diffraction Tomography: Scanning microbeam diffraction (μXRD) and microbeam fluorescence (μXRF) tomography experiments of the pristine VPO catalyst examined in the main text were carried out at the microXAS beamline of the Swiss Light Source (SLS), Paul Scherrer Institut (PSI), Switzerland. For μXRD & μXRF experiments an 11.3 keV incident beam was focused with a Kirkpatrick–Baez (KB) mirror system to a size of ~1 × 1 (H × V) μm^2. For microbeam X-ray fluorescence, XRF spectra were collected using two Si drift diode detectors (KETEK), which were placed at opposite sides of the sample perpendicular to the direction of X-ray propagation. Using two detectors on opposite sides of the sample helps alleviate self-absorption effects on the tomography reconstruction. Diffraction patterns collected from LaB_6 powder were used to calibrate the sample-to-detector distance. The detector, an Eiger 4M, was positioned about 8.3 cm from the sample. After aligning the tomography pin with the sample stage's center of rotation, we simultaneously recorded XRD patterns and XRF signals.

Several tomographic slices across the sample height of the pristine catalyst, with a vertical step size of 1 μm, were reconstructed from a series of horizontal line scans, during which the sample was scanned through the X-ray beam with a step size of 0.5 μm. 61 angular projections were acquired per tomographic slice. In case of the acquired XRF, spectra was integrated in the energy range of the V *K*α signal in order to obtain a single sinogram per axial slice. A simultaneous iterative reconstruction technique (SIRT)(66) algorithm was then applied to obtain the tomographically reconstructed volume. The diffraction tomograms were obtained similarly, for those the measured diffraction patterns at each scanning point were first azimuthally integrated using the Bubble interface of PyFAI(67). The one-dimensional diffraction patterns were next analyzed as a function of position and rotation to construct one sinogram per 2θ value, generating a total of about ~4000 sinograms covering a total range of 1.5–56° in 2θ with a step size of ~0.01°. Smaller 2θ angles, and the transmitted intensity, were recorded by a SiC diode, which was integrated to the 2 mm diameter beamstop. Following tomographic reconstruction, this procedure allowed the acquisition of the full powder-XRD pattern per voxel of the tomographically reconstructed volume.(68) Voxel-level diffraction patterns were fitted using XRDUA for phase identification.(69) We refrained from any voxel-level refinement operations due to insufficient data quality. Please see Figure S10, for visualizations of both the μXRF and μXRD tomograms.

Micro X-ray Absorption Near-Edge Spectroscopy (μ-XANES): μ-XANES measurements of the pristine VPO catalyst pillar were similarly acquired at the MicroXAS beamline of the SLS, PSI. A beam focused with a Kirkpatrick–Baez (KB) mirror system to a size of ~0.7× 0.7 (H x V) μm^2 was used. A photon energy range of 5400-5600 eV or across the V *K*-edge was used for the XANES measurements. Data were acquired in 0.3 eV steps using the aforementioned beamstop-integrated SiC diode placed behind the sample. For each incident photon energy we collected one line scan across the pillar width, for which the sample was scanned in lateral direction in steps of 0.5 μm. The acquired spectra were next averaged and the resulting V *K*-edge XANES were processed using Athena.(42) Resonant-edge energy determination followed IFEFFIT's algorithm, used to find the first peak of the first derivative of μ(E).(42) Please see Figure S14 for the obtained spectra.

Selective Oxidation of n-Butane to Maleic Anhydride (MA), its Industrial Realization and Relevance:

The selective oxidation of *n*-butane to maleic anhydride ($C_4H_2O_3$) and its chemical derivatives maleic acid and fumaric acid over vanadium phosphorus oxides (VPO) was industrially first realized by Monsanto in 1974. These chemical intermediates find use in nearly all areas of chemistry, most prominently in the production of unsaturated polyester resins, i.e. the production of household and industrial plastics. Given the continuing demand in the former, the annual production of maleic anhydride is continuously increasing, exceeding 2 million tons by 2020.(23, 24) This important catalytic conversion process operates under kinetic control. The exothermic conversion of *n*-butane to maleic anhydride over vanadium phosphorus oxides in presence of oxygen possesses two main reaction by-products in the form of carbon monoxide and carbon dioxide. Both of which are thermodynamically more favorable, Figure S1. This leads to strict requirements on the catalyst concerning thermal and chemical stability and the reactor with regards to heat transfer capacities to provide a constant reaction environment, e.g. temperature and feed composition. The current generation of heterogeneous catalysts and reactors exhibit maleic anhydride yields of ~ 60%.(26)

Industrial conversion is frequently carried out in fixed-bed reactors, operating at roughly 400°C. These reactors consist of a series of actively cooled reactor tubes (>10,000 tubes; with an inner diameter of ~20 mm), filled with porous VPO catalyst bodies or pellets. Pressurized, preheated mixtures of air, *n*-butane (< 2 vol.%), and water (< 3 vol.%) are continuously fed through the reactor tubes from the bottom. Reaction products are syphoned off from the top and further cycled for refinement purposes in selected cases.(26) Due to known catalyst deactivation mechanisms, commonly registered in the form of decreasing yield and selectivity as well as a decreasing phosphorus to vanadium ratio in the catalyst bodies, additionally added to the feed-stream is a trialkyl phosphate ester at concentrations up to 10 ppmv. The industrial VPO catalysts utilized in these fixed-bed reactors are generally of the porous bulk type, i.e. predominantly composed of vanadium phosphate phases such as vanadyl pyrophosphate and prepared from precursors such as vanadyl hydrogenphosphate hydrates ($VO(HPO_4)(H_2O)_n$) by thermal pre-treatment at ~500°C in an inert atmosphere. While catalysts based on vanadyl pyrophosphate possess a nominal ratio of phosphate to vanadium of 1, catalysts are generally prepared with an over-stoichiometric amount of phosphate by means of phosphate dosing during synthesis, as catalytic peak performance is observable at bulk P/V ratios of roughly 1.1. The additional phosphate is, among other opinions, believed to be present in form of vanadium-rich amorphous metaphosphate. The latter is poorly bound to crystalline vanadyl pyrophosphate stabilizing exposed V^{4+}.(23) Notably, pristine catalysts may contain up to 30% of amorphous material which may explain the frequent observation of higher-than-expected sample-averaged vanadium oxidation state, i.e. vanadyl (VO_2) groups in the catalyst may exist as V^{5+} defects.(25) (26-29)

Suggested Active Sites in VPO Catalysts:

Modeling studies have suggested that the P=O bond is the active site for initiating the VPO chemistry, by extracting the H from the *n*-butane C–H bond.(33) The ability of P=O to cleave alkane C–H bonds arises from a mechanism that decouples the proton transfer and electron transfer components of this H atom transfer reaction. The study's authors demonstrated that placement of a highly reducible V^{+5} next to the P=O enhances the activity of the P=O bond to extract the proton from an alkane, while simultaneously transferring the electron to the V to form V^{+4}. As such, introducing a VO vacancy thus makes the P=O bonds have more uncompensated negative charge, and, therefore, have higher affinity to the H in butane. It is fair to assume, then, that the defected structure shown in the main text will show high activity in the conversion process of *n*-butane to maleic anhydride.

Ptychographic Computed X-ray Tomography and Sensitivity to Variations in Incident Energy:

Ptychographic X-ray computed tomography (PXCT)(22) is a combination X-ray ptychography and computed tomography. Ptychography is a lensless imaging technique in which the phase problem is solved by means of iterative phase retrieval algorithms.(70) During a ptychographic scan, or the acquisition of a tomographic projection, the sample is scanned at positions where the incident illumination overlaps. At each scanning point a far-field diffraction pattern measured. By reconstructing these diffraction patterns together and leveraging the illumination overlap the solution of the phase problem becomes well constrained. By applying ptychography at different projection angles, i.e. sample orientations, PXCT is able to retrieve the complex-valued refractive index distribution, n, of the imaged sample. This provides tomograms of both phase and amplitude contrast whose spatial resolution is not limited anymore by the imaging optics but the angular extent to which the specimen-scattered intensity can be detected.(22) Solution of the phase problem in conjunction with the removal of resolution-limiting optics allows PXCT to provide us with quantitative phase and absorption tomograms of high spatial-resolution and signal to noise ratio when compared to other state of the art X-ray microscopy techniques.

PXCT measurements are commonly conducted far from any sample-relevant absorption edges, i.e. resonant energies, to allow the conversion of the phase tomogram, i.e. the real part of the refractive index decrement, δ, to electron density, n_e, as well as the conversion of the amplitude tomogram, i.e. the imaginary part β of the refractive index to absorbance, μ.(57) However, it is worth to remember that δ and β can be expressed as the real and imaginary parts of the atomic scattering factor, i.e. $f_0 = f_1 + if_2$; which are known to be energy dependent. As such it comes to no surprise that the refractive index distributions retrieved by PXCT are equally sensitive to changes in the respective scattering factor, Δf_E, at or near sample-relevant absorption edges, Figure S14.(57)

$$n = 1 - \delta - j\beta = 1 - \frac{r_e}{2\pi}\lambda^2 \sum_k n_{at}^k \ (f_1^k + if_2^k) \tag{S1}$$

This energy dependence is commonly used in techniques such as X-ray absorption near-edge spectro- (XANES) tomography, (8, 13) in which a series of tomograms are measured across a selected absorption edge to localize and characterize the chemical nature of the edge-specific element in the specimen. Such applications using PXCT are still rare, despite the advantages PXCT offers as base tomography technique, i.e. dose efficiency, high spatial-resolution, easier access to the quantitative hyperspectral information. Despite these advantages PXCT is not used for transmission spectroscopy due to multiple interlinked factors, being predominantly: the extensive acquisition time of a single high-resolution PXCT dataset which can be more than 8 hours for a 15 μm diameter sample at 20 nm spatial resolution, the limited amount of available beamtime at PXCT-capable synchrotron beamlines, radiation damage, and physical stability of the experimental setup and the sample during tomogram acquisitions. Factors, which made these measurements previously practically impossible, henceforth forcing prior demonstrations examples to compromise either on the field of view, the energy range and/or the energy sampling,(14, 57, 71) i.e. the total number of energies at which tomographic projections are collected across an absorption edge. The here shown introduction of sparse angular sampling reduces the acquisition time by an order of magnitude while retaining nm spatial resolution and sufficient spectral resolution, which establishes sparse X-ray transmission near-edge spectro (XTNES) tomography as a viable tool for quantitative chemical speciation on the nanoscale in 3D.

The basis of this sparsity implementation in the context of X-ray spectro-tomography acquisition is rooted in the nature of spectral signal changes being inherently correlated. From a signal perspective, it is then clear that the information content in a hyperspectral volume does not require Crowther sampling for each energy if appropriate reconstruction methods are applied as in the presented case.

Local Structure Optimization:

All ground-state total energy calculations in this work have been performed with the all-electron full-potential DFT code FHI-aims.(72, 73) Electronic exchange and correlation was treated with the PBE functional.(74) Geometry optimization was done with the "tier2" atom-centered basis set using "tight" settings for numerical integrations. Local structure optimization is done using the Broyden-Fletcher-Goldfarb-Shanno method relaxing all force components to smaller than 10^{-2} eV/Å. DFT calculations presented in the current manuscript relied on the automatic optimization of the spin states as implemented in the FHI-aims package. All structures presented correspond to the singlet spin state.

In the case of the "ideal" vanadyl pyrophosphate crystal, the experimental unit cell parameters (a = 7.738 Å, b = 9.587 Å, c = 16.589 Å) were used. In the case of the defected structure, with one $[(VO)_2]$ element missing, the full reoptimization of the unit cell parameters has been conducted. The resulting unit cells parameters were: a = 8.310 Å, b = 9.683 Å, c = 16.041 Å.

We have a relatively large size of the unit cell, this is because the periodic model of the vanadyl pyrophosphate crystal has a stoichiometry of $[(VO)_2]_8[P_2O_7]_8$, comprising 104 atoms, and the fact that all electrons are accounted for explicitly, 1184 electrons in total in the case of an "ideal" crystal. Therefore Brillouin zone integration was performed with a reciprocal space mesh consisting of only the gamma point. The size and the location of the $[(VO)_2]$ vacancy was chosen based on the experimental data on vanadium to phosphorus ratio, vanadium concentration, vanadium oxidation state, and the total electron density in the unit cell.

Supplementary Figures

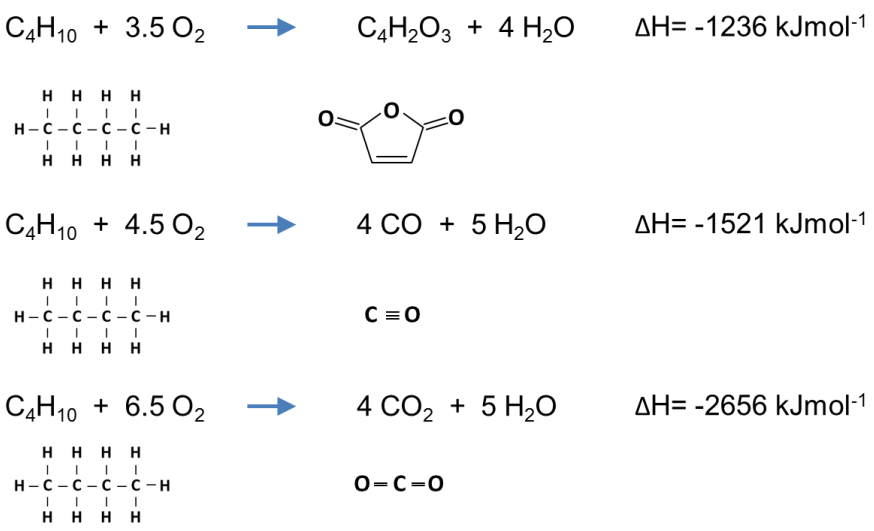

Supplementary Figure S1: Oxidation of n-Butane to Maleic Anhydride and The Thermodynamically More Favorable By-Products.(26)

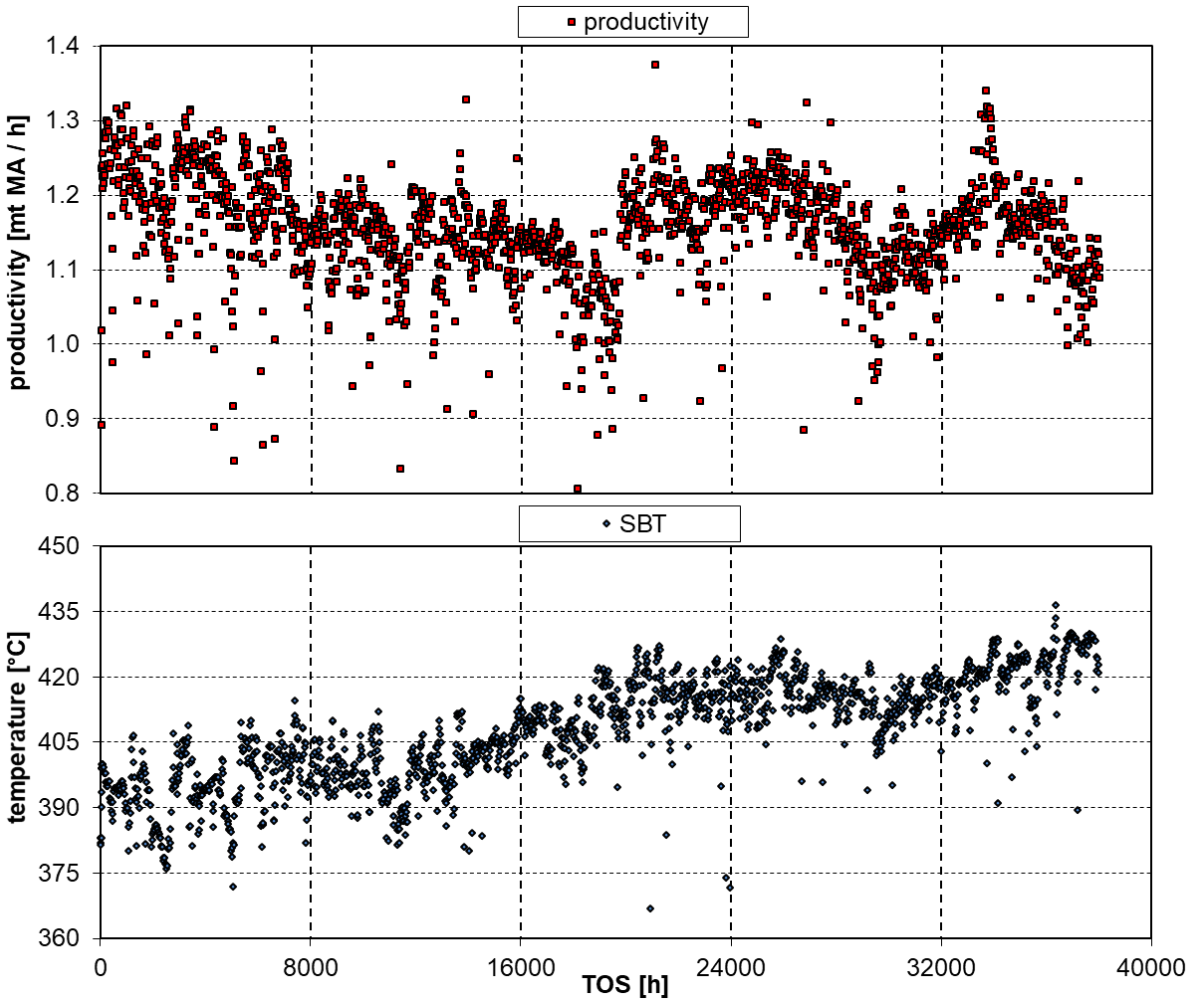

Supplementary Figure S2: VPO Catalyst Performance over Catalyst Lifetime in an Industrial Fixed-Bed Reactor. Shown in (a) are industrial catalyst productivity data in metric tons of MA per hour (red squares), of the studied catalyst in the main text. Provided in (b) is the reactor's salt bath temperature (SBT -blue rhombs) or temperature over the catalyst lifetime or time on steam (TOS). Using XTNES tomography we examined a VPO catalyst at the first and last time point.

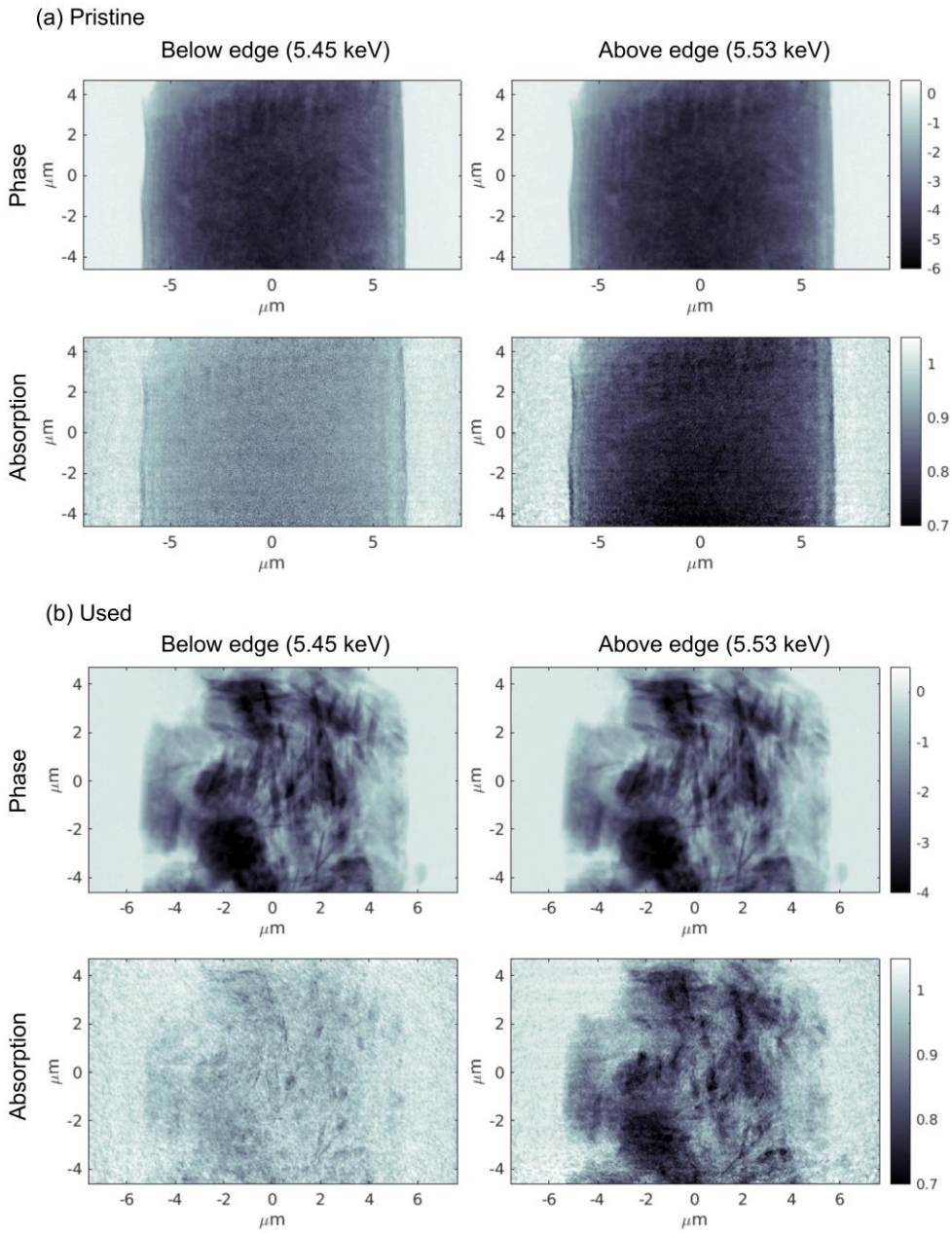

Supplementary Figure S3: Example of Reconstructed High-Resolution Ptychography Images Utilized in the Tomographic Reconstruction Process. Shown are typical reconstructed ptychography images (tomographic projections) acquired for both samples. (a) Images of the pristine catalyst sample and (b) the used catalyst sample are acquired below the V *K*-edge at 5.45 keV and above the edge at 5.53 keV. Shown are both the phase (top rows) and amplitude component (bottom rows). All complex-valued tomographic projections used in this study can be downloaded from DOI [10.5281/zenodo.4505125].

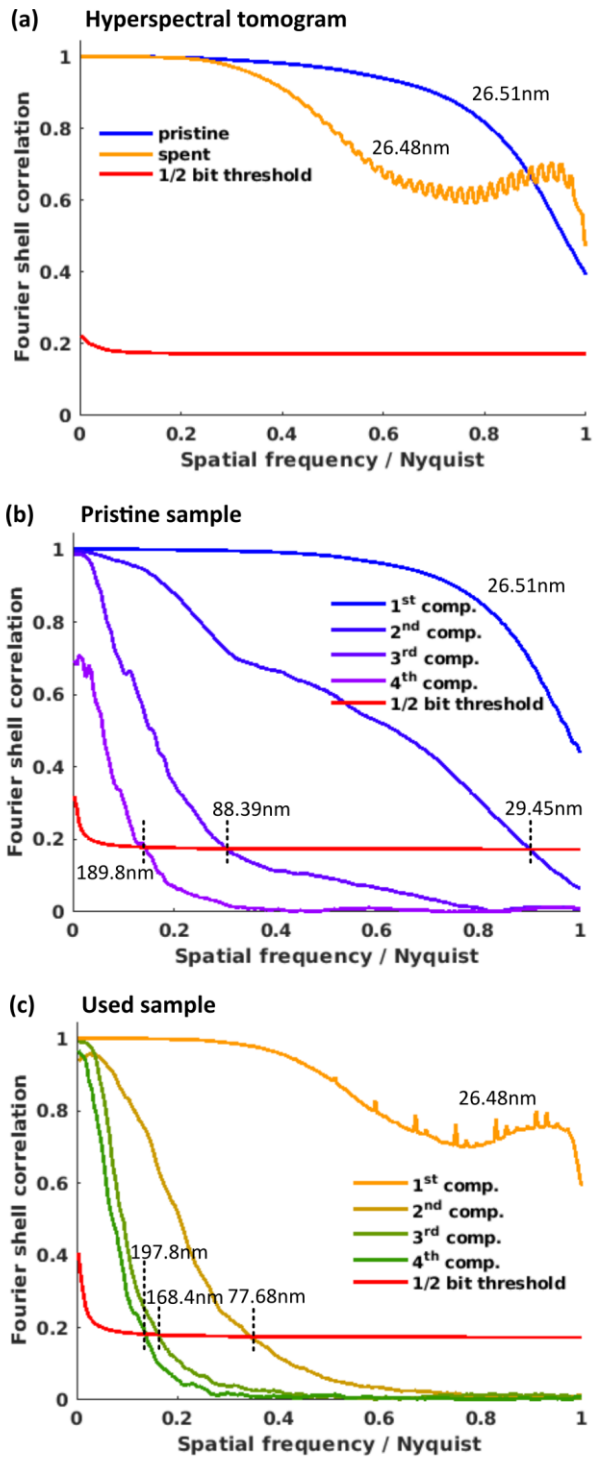

Supplementary Figure S4: Fourier Shell Correlation (FSC) of XTNES Tomograms. Provided are FSC curves of the 4D hyperspectral tomograms, according to Eq. (1) in the main text, for the pristine and used catalyst. (a) FSC curves for the entire hyperspectral tomograms alongside resolution estimates. Both the pristine and the used catalyst tomogram reached a voxel-size-limited half-pitch spatial resolution. The tomogram voxel sizes are 26.51 nm for the pristine and 26.48 nm for the used catalyst. FSC curves of the first 4 component tomograms, $X_k(\mathbf{r})$, and the corresponding half-period resolution estimates are shown in (b) for the pristine and (c) for the used catalyst sample.

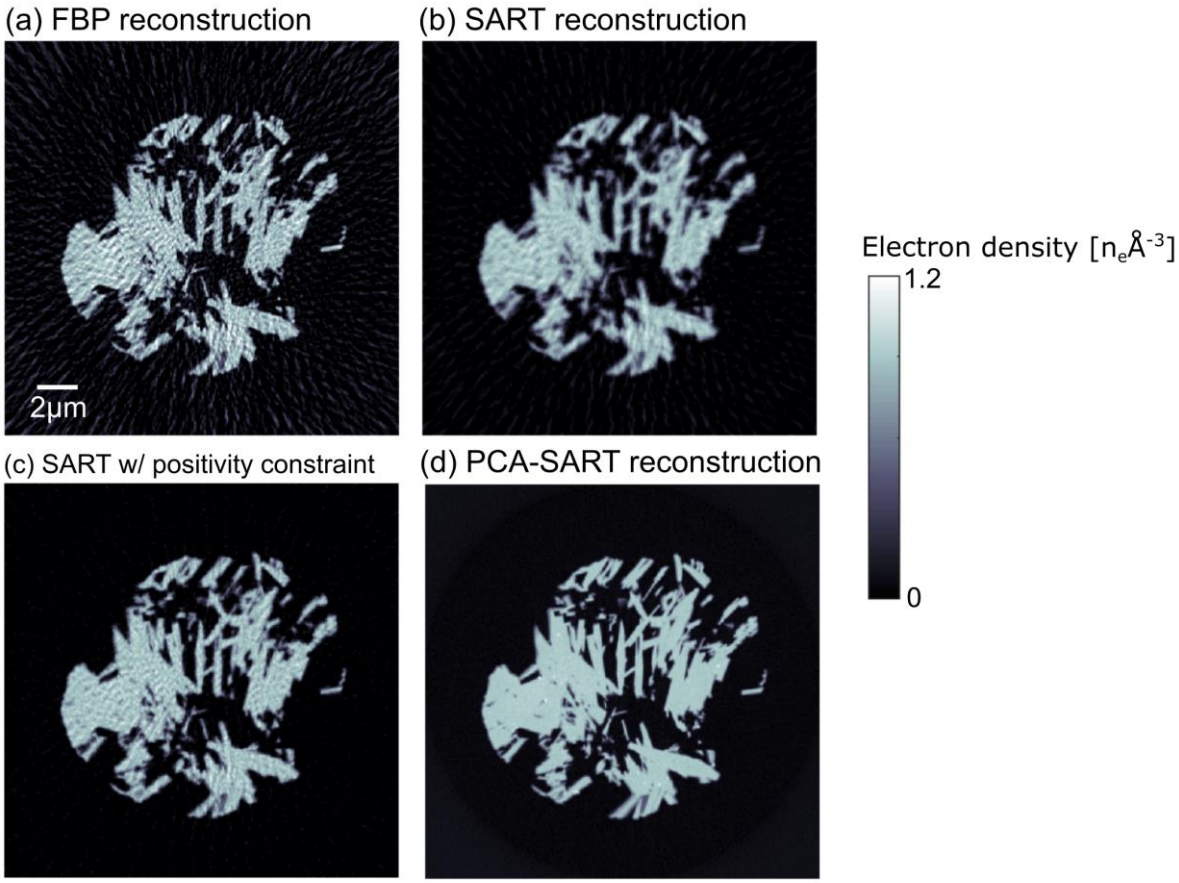

Supplementary Figure S5: Comparison of Analytical and Iterative Tomogram Reconstruction Methods. Shown is a comparison of common analytical and iterative tomogram reconstruction methods and the here introduced method, which leverages the sparsity of information in a hyper-spectral tomogram. Specifically compared are axial orthoslices of electron density tomogram reconstructions of the used VPO catalyst, at 5.451 keV, using different reconstruction methods: (a) the conventional filtered back-projection (FBP) method was used as an example of analytical reconstruction methods, (b) iterative SART method without constraints and (c) SART method with positivity constraint. Tomogram reconstructions shown in (a) to (c) were obtained using all 68 equal angular sampled projections of identical illumination energy. Shown in (d) is the XTNES reconstruction of the electron density at the same energy utilizing the entire sparse spectral-tomogram dataset.

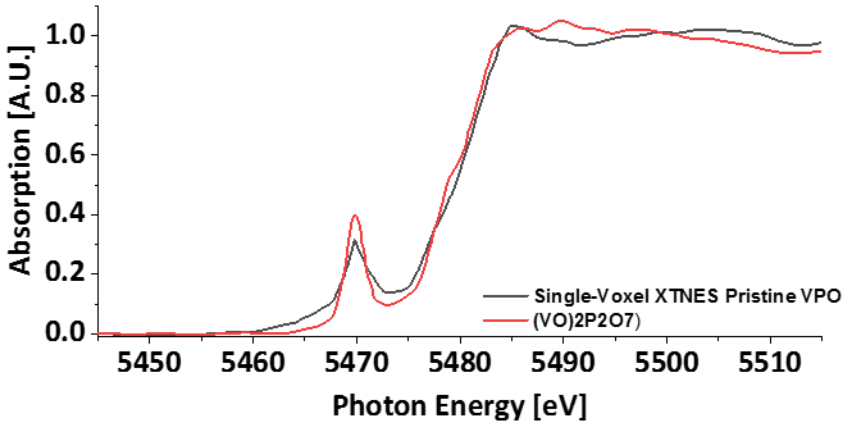

Supplementary Figure S6: Comparison of a Voxel-level Vanadium *K-edge* Absorption Spectra Extracted from the Pristine VPO XTNES Tomogram with a Literature Reported Vanadium *K-edge* Absorption Spectra a VPO Catalyst Component. The voxel-level absorption spectra were obtained from the high-resolution phase spectra following a Kramers Kronig transformation. The voxel-level spectra is best described by a spectra of vanadyl pyrophosphate as reported in Ruitenbeck.(26) See Figure 2C(x) for the approximate location of the voxel in the XTNES tomogram.

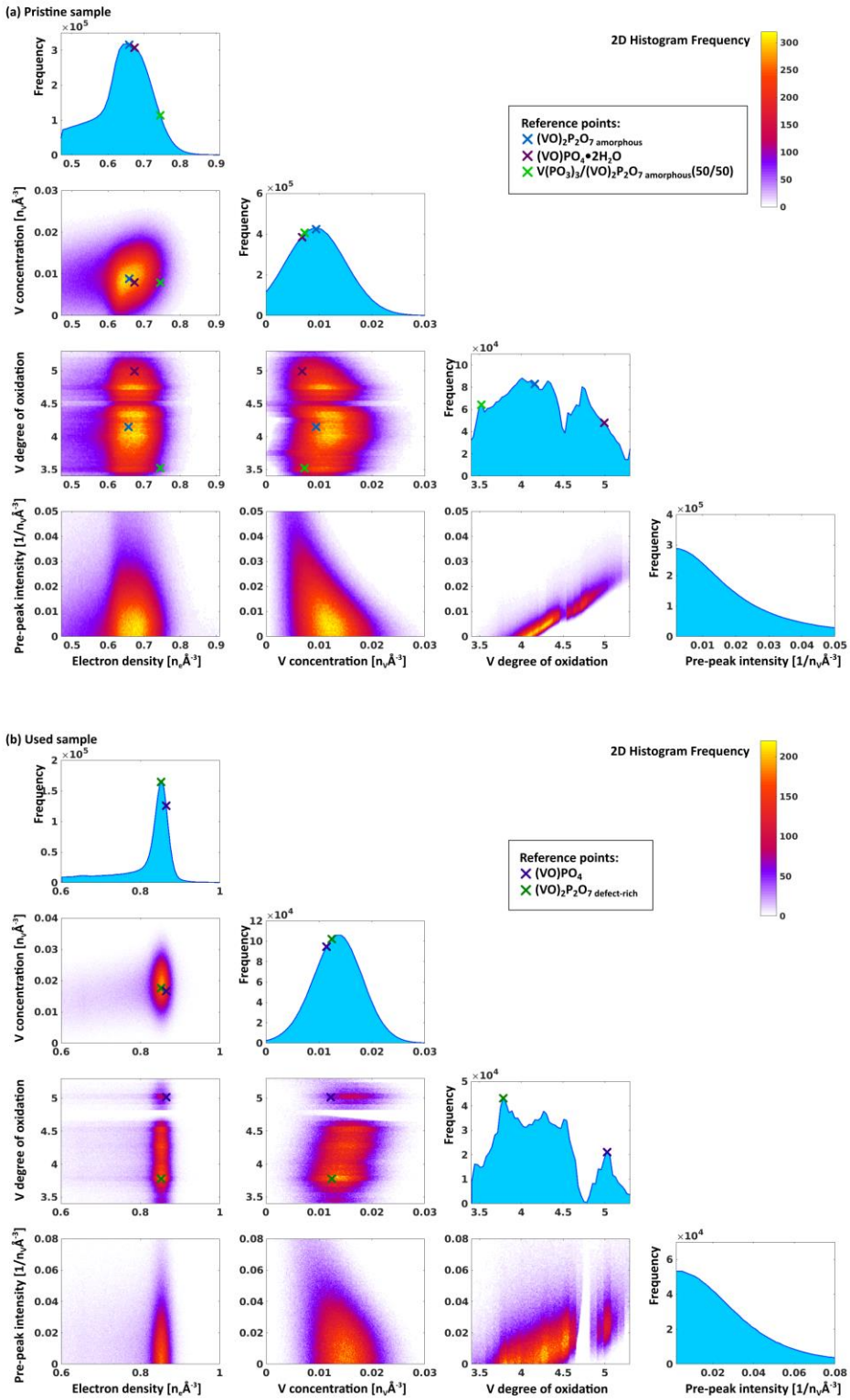

Supplementary Figure S7: Histogram and Correlative Bivariate Histograms of Electron Density and Chemical Information Extracted from the XTNES Tomogram. (a) Pristine and (b) used catalyst. See Method section in Supplementary Materials for details on chemical speciation. Compositional reference values of identified catalyst components, such as $(VO)PO_4$, $(VO)PO_4 \cdot 2H_2O$, $V(PO_3)_3$, $(VO)_2P_2O_{7\ \text{defect-rich}}$, $(VO)_2P_2O_{7\ \text{amorphous}}$ are marked in the histograms or listed explicitly in Table S2.

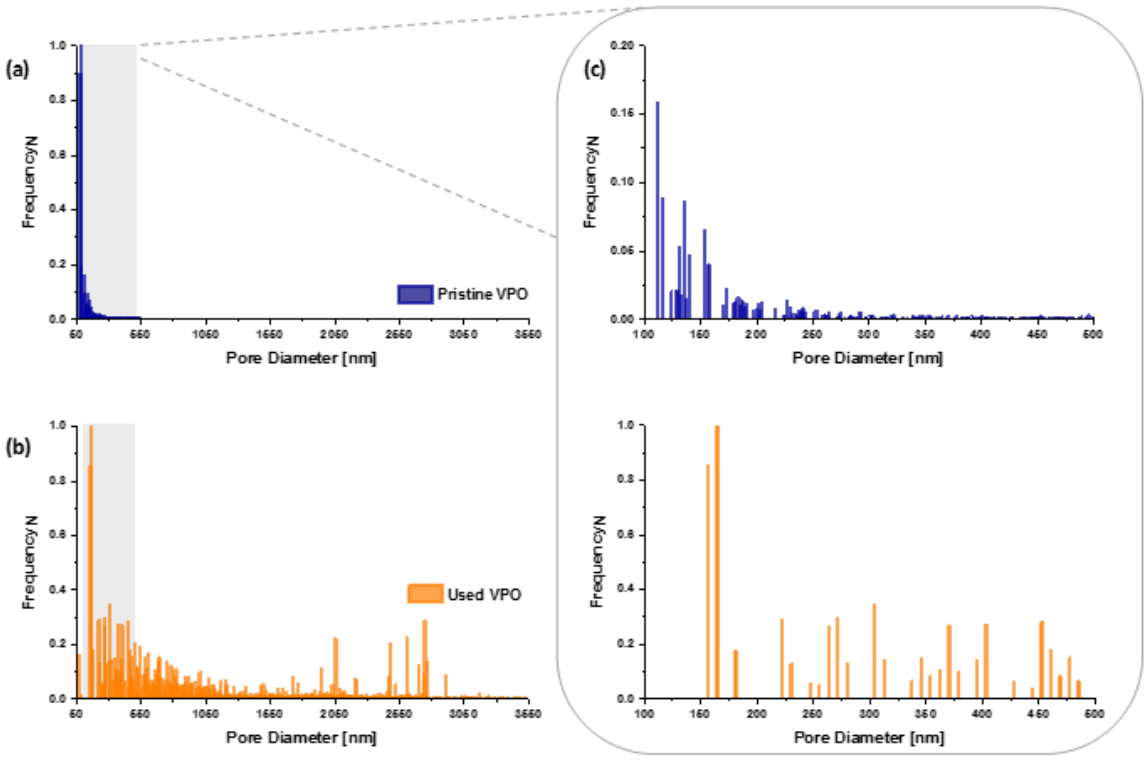

Supplementary Figure S8: Pore Size Distributions and Pore Network Connectivity. Pore size distributions (PSD) of (a) the pristine and (b) the used VPO catalyst, extracted from the electron density tomogram by means of 3D thickness-map calculations. (c) Zoom of the 100-500 nm pore range for both samples. The zoom corresponds to the grey shaded area in (a) and (b). The smallest pores considered were 52 nm in diameter, which corresponds to two half-period resolution elements. For the case of the pristine catalyst the 5 biggest pore networks comprise roughly ~60 vol.% of the total pore volume.

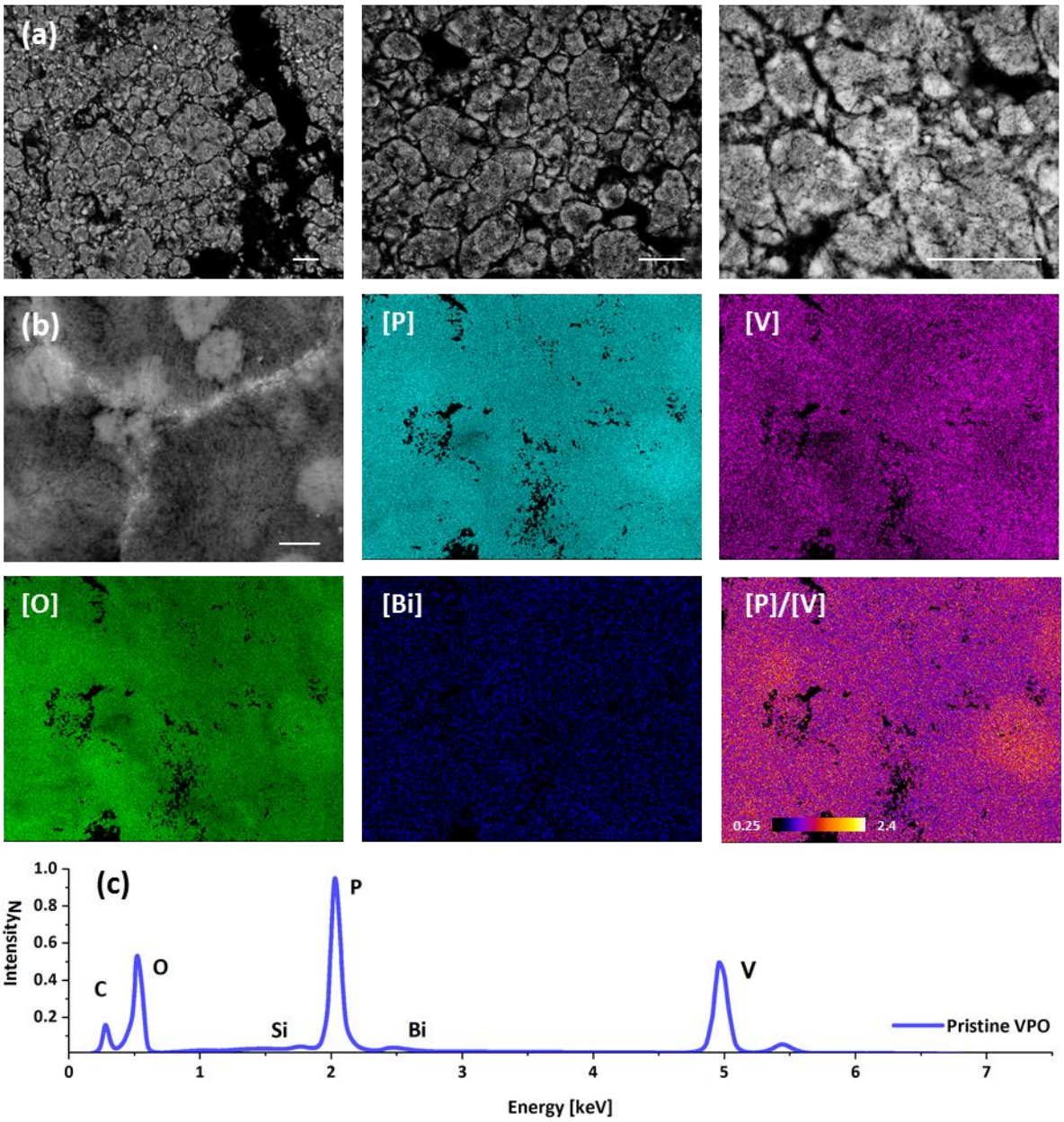

Supplementary Figure S9: Scanning Electron Microscopy of a Pristine Industrial VPO Catalyst. (a) SEM micrographs recorded with backscattered electrons at increasing magnification. Scale bars are 10 µm. (b) SEM image and energy-dispersive X-ray (EDX) spectroscopy maps of P, V, O and Bi, and an overlay of P and V EDX maps. Scale bar 1 µm. (c) Area averaged normalized (N) EDX spectra.

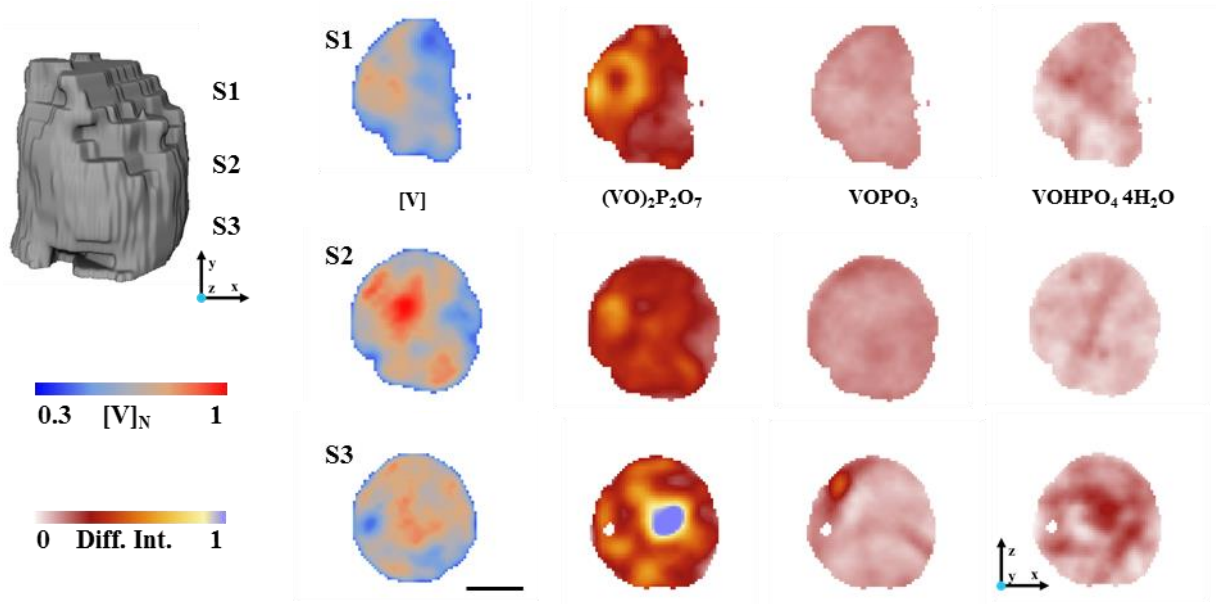

Supplementary Figure S10: Micro X-ray Fluorescence and Diffraction Tomography of a Pristine Industrial VPO Catalyst. Shown is a volume rendering of the imaged pristine catalyst and axial orthoslices of both the acquired vanadium distribution obtained by means of XRF tomography and main crystalline catalyst components obtained through XRD tomography. Provided orthoslices, S1-S3, were taken at different heights across the catalyst to highlight variations in vanadium concentration and composition. Scale bar is 5 µm.

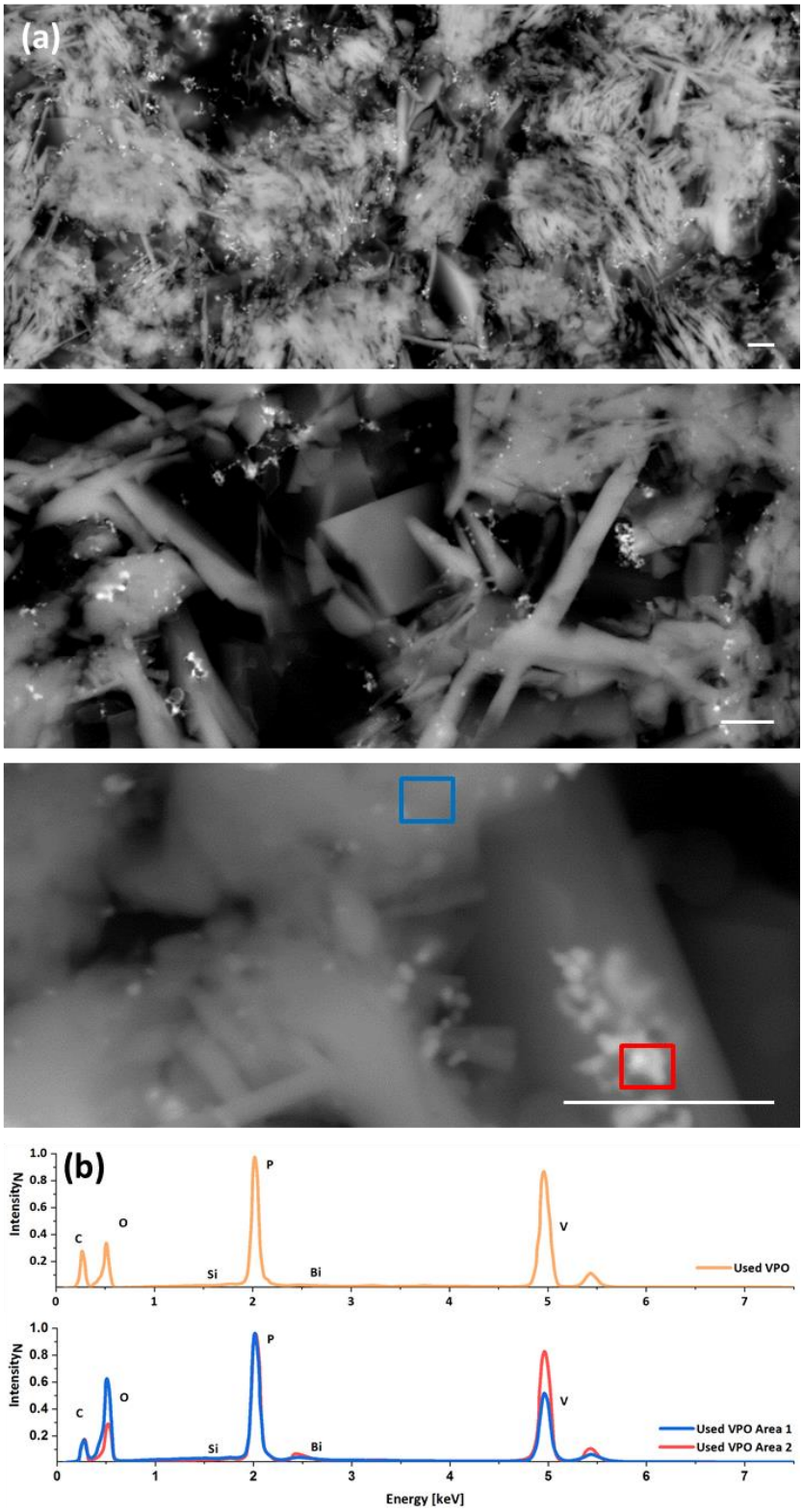

Supplementary Figure S11: Scanning Electron Microscopy of a Used Industrial VPO Catalyst. (a) SEM images recorded with backscattered electrons at increasing magnifications. Scale bars 1 µm. (b) Energy-dispersive X-ray (EDX) spectra collected of a large area (top, P/V ~ 1) and of the areas indicated in (a) either rich in added phosphate moderator during operation (blue frame) or Bi dopant particles rich and moderator poor (red frame, P/V ~ 0.8).

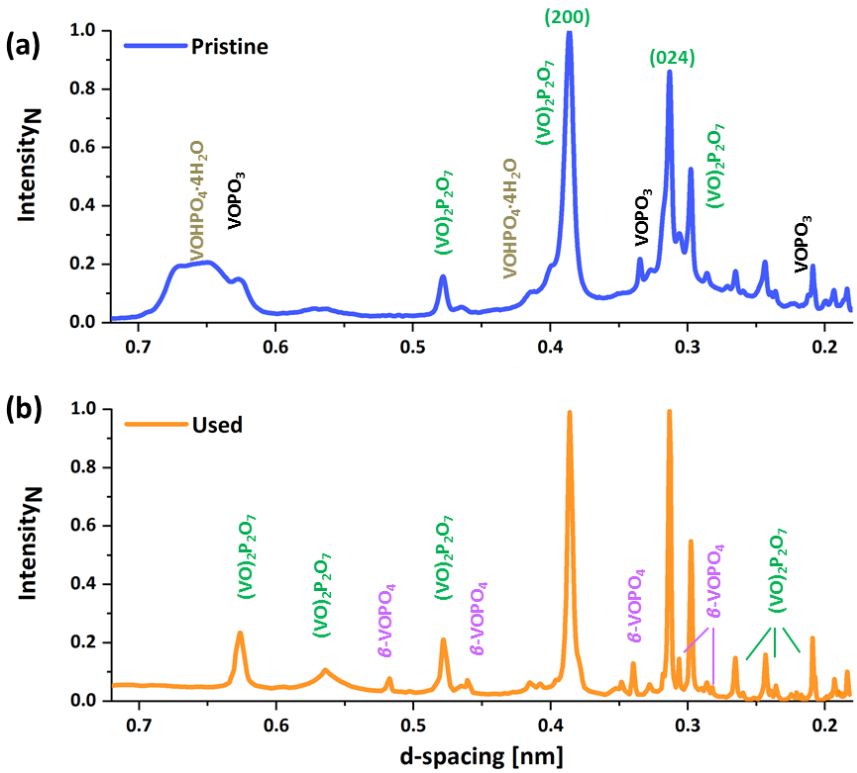

Supplementary Figure S12: Powder X-ray Diffraction of Industrial VPO Catalysts. Sample population averaged PXRD patterns of a (a) pristine and a (b) used industrial VPO catalysts. Prominent peaks of crystalline catalyst components are highlighted. Note the significant amorphous or nano-crystalline background in the pristine sample, compared to the used catalyst sample. This background comprises ~ 30 % of the total integrated intensity, which is in agreement with the observed spread in electron density, vanadium concentration, and speciation in the pristine catalyst seen in the XTNES tomograms. According to Rietveld refinements, with a goodness of fit (R^2) of ~1.9, the detectable crystalline material in the pristine catalyst is dominantly composed of orthorhombic $(VO)_2P_2O_7$ (~94 wt.%), $VOHPO_4{\cdot}4H_2O$ (~5 wt.%) and $VO(PO_3)_2$ (~1 wt.%). The used catalyst of orthorhombic $(VO)_2P_2O_7$ (>95 wt.%) and β-$VOPO_4$ (~5 wt.%). Both the disappearance of amorphous material and the detection of, V^{5+} containing, β-$VOPO_4$ in the deactivated catalysts as well as the structural changes of $(VO)_2P_2O_7$ are in agreement with the structural reorganization and phase transformations found by XTNES tomography. The aforementioned structural changes of $(VO)_2P_2O_7$ include an increase in crystalline domain size from ~250 nm to greater 1 µm, an overall increase in microstrain (µε), from 1.5 to 400, as well as a ~10% increase in the Bragg reflection intensity ratio of $(VO)_2P_2O_7$ between the {024} and the {200} reflection in the used sample. A change potentially reflective of a decrease in exposed, selective oxidation active, vanadyl groups, see also Figure 3 in the main text.(28)

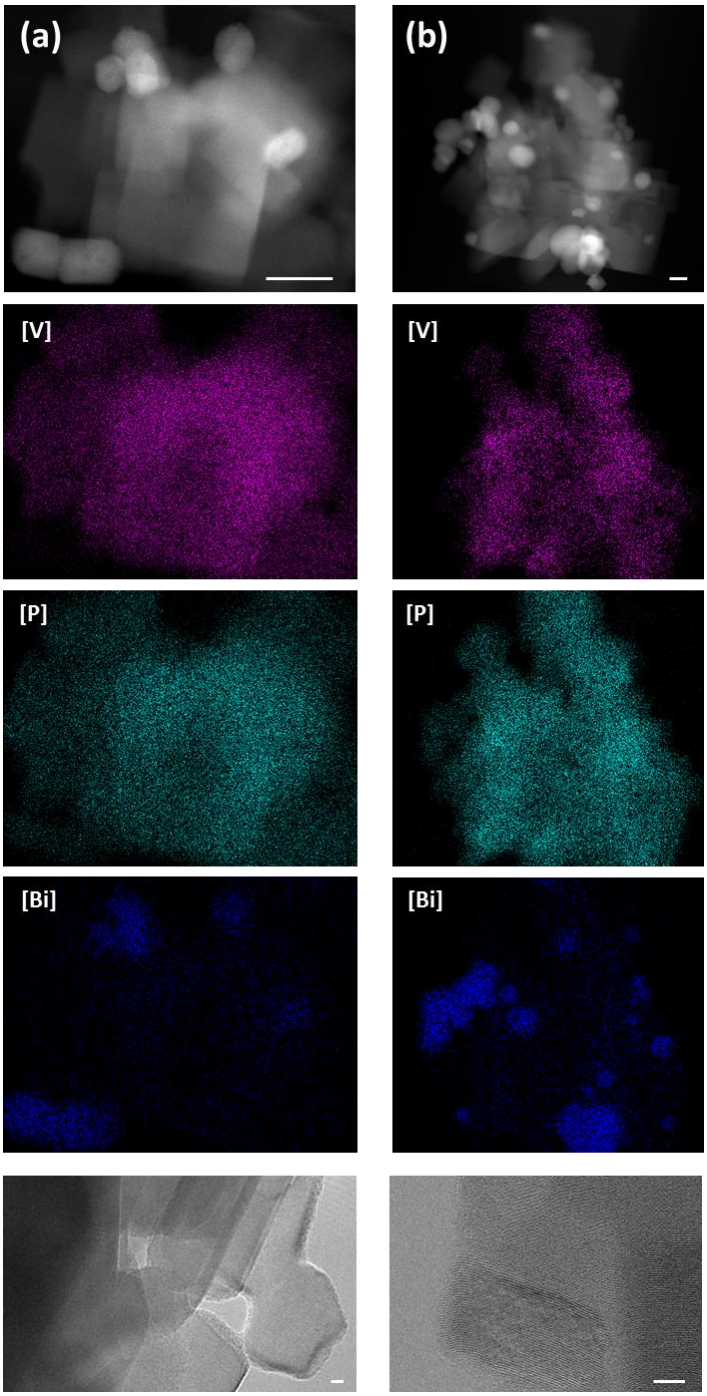

Supplementary Figure S13: Transmission Electron Microscopy of Industrial VPO Catalysts. Combination of HAADF-STEM micrographs (top, scale bars 50 nm), corresponding energy-dispersive X-ray (EDX) maps, and high-resolution TEM images showing lattice fringes (bottom, scale bars 5 nm) of the main catalyst component collected of a (a) pristine and a (b) used VPO catalyst. Average lattice spacing in (a) is ~0.738 nm, in agreement with the {001} reflection of $VOHPO_4 \cdot 4H_2O$ and (b) the {200} reflection of $(VO)_2P_2O_7$.

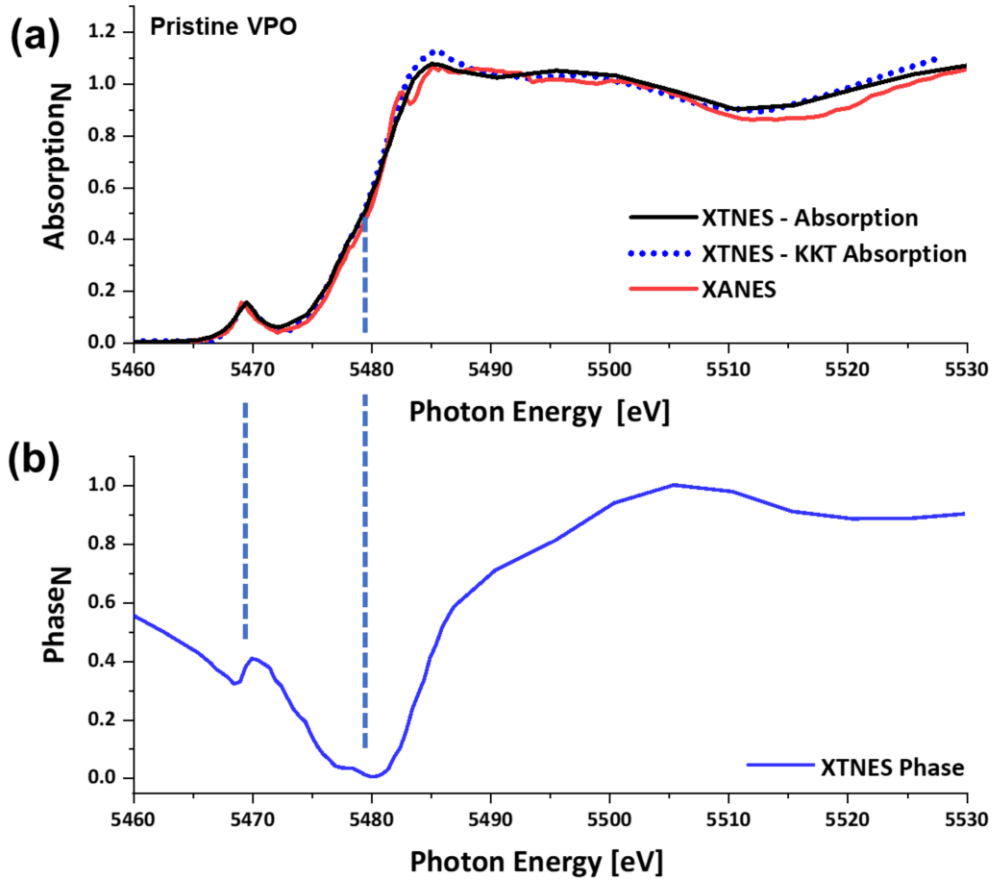

Supplementary Figure S14: Sample-Averaged Normalized Vanadium *K*-edge Absorption and Phase Spectra of the Pristine VPO Sample. (a) Comparison between sample-averaged absorption spectrum from the ptychography XTNES absorption component (black); the absorption spectrum resulting from a Kramers-Kronig transformation of the XTNES phase component (blue, dashed); and XANES spectrum measured at the MicroXAS beamline of the SLS using a dedicated X-ray absorption spectro-microscopy setup (red). (b) Average phase spectrum from XTNES tomography. All spectra were normalized (N) to a post-edge value of 1 for comparison purposes. While minor differences across the absorption spectra are visible, absorption edge and pre-peak position as well as pre-peak intensity are well matched across the techniques and/or following a KKT of the phase spectra.

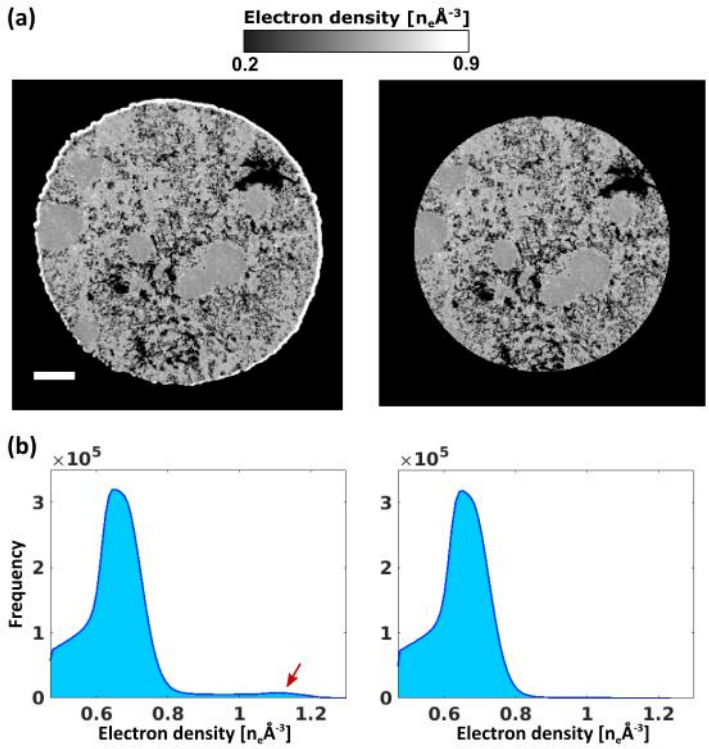

Supplementary Figure S15: Cylindrical Mask Applied to the Pristine VPO XTNES Tomogram. (a) Axial slice of the electron density of the pristine VPO XTNES tomogram before (left) and after (right) masking. (b) Electron density histograms of the whole sample volume before and after masking. The red arrow highlights the higher electron density bump removed by masking out the outermost 200 nm.

Supplementary Table S1: Structural and Chemical Makeup of Reference Compounds.

Compound	Electron Density	[V]	V *K*-Edge	Pre-Edge*	[P]/[V]	Oxidation State	Geometry†
	n_e Å^{-3}	n_V Å^{-3}	eV	r.l.	/		
V_{metal}	1.58	0.068	5465			0	
Bi_{metal}	2.35						
Bi_2O_5	1.71						
$BiPO_4$	1.63						
H_3PO_4	0.58						
V_2O_3(29)	1.37	0.039	5475.7	Very Weak	-	3	O
VO_2	1.29	0.033	5478.1	Moderate	-	4	O
V_2O_5(29)	0.96	0.022	5480.9	Strong	-	5	P
$(VO)_2P_2O_{7\ crystalline}$(26)	0.96	0.013	5478.7		1	4	O
$(VO)_2P_2O_{7\ V5+\ defect\text{-}rich}$(26)	~0.88	~0.012	~5478.7		1	4 & 5	
$(VO)_2P_2O_{7\ amorphous}$(26)	~0.66	~0.009	~5478.7		1	4 & 5	
$V(PO_3)_3$	0.83	0.007	5474.4	Very Weak	3	3	O
$VO(PO_3)_2$-α(75)	0.89	0.016	5475.6	Very Weak	2	4	O_d
$VO(PO_3)_2$-β(76)	0.85	0.015	5475.9	Very Weak	2	4	O_d
$V_2O(PO_4)$	1.09	0.021	5476.1	Weak	1	4	O
$VO(HPO_4)\cdot 4H_2O$	0.68	0.0057			1	4	O_d
$VO(HPO_4)\cdot 2H_2O$-α	0.75	0.007			1	4	O_d
$VO(HPO_4)\cdot 2H_2O$-β	0.69	0.007	5476.9	Moderate	1	4	O_d
$VO(HPO_4)\cdot 0.5H_2O$(77)	0.89	0.009			1	4	O_d
$VO(HPO_4)$ (78)	0.90	0.001			1	4	O_d
$(VO)PO_4\ 2H_2O$(79)	0.68	0.007	5482.8	Strong	1	5	O_d
$(VO)PO_4$-α	0.96	0.012	5482.5	Strong	1	5	O_d
$(VO)PO_4$-β	0.94	0.012	5482.5	Strong	1	5	O_d

The electron density and vanadium concentration of reference compounds were calculated using tabulated molecular weight and mass density values. Oxidation state and coordination geometry information were extracted from listed references in the first column.(29) *Relative pre-peak intensities are compared to listed vanadium oxides of distinct oxidation states. †O-octahedral, T-tetrahedral, P-square pyramidal, d-distorted.

Supplementary Table S2: Properties and Composition of Pristine and Used Industrial VPO Catalysts.

Sample	Pristine	Used
Bulk Analysis		
Composition		
Bismuth Bi [wt.%]	2.0	1.30
P/V	1.075	1.038
Total Surface Area [m^2g^{-1}]	~20	~6
Total Porosity [%]	43	52
Average Pore Diameter [nm]	33	187
Mean Vanadium Oxidation State	4.08	4.02
Ptychographic X-ray Transmission Near-Edge Spectro Tomography#		
Total Porosity [%]	~40	~57
Average Pore Diameter [nm]	~85	~185
Mean Vanadium Oxidation State	4.086	4.036

Bulk Analysis: Data were provided by Clariant AG. **Ptychographic X-ray Transmission Near-Edge Spectro Tomography:** # Provided estimates are subject to finite image resolution and image-segmentation limitations. The resolution of the sparse XTNES tomograms allows for imaging > 80 % and > 90% of the total catalyst pore volume for the used and pristine samples, respectively. For average pore diameter calculations, a pore diameter of 52 nm was the considered lower limit.

Supplementary Movies S1 and S2: Volume Rendering of and Orthoslices Through XTNES Tomograms. Shown are volume rendering and cut slice animations of the hue-saturation-value renderings presented in Figure 2 of the main text.

REFERENCES AND NOTES

1. J. R. Ebner, M. R. Thompson, in *Studies in Surface Science and Catalysis* (Elsevier, 1991), vol. 67, pp. 31–42.

2. D. D. Chung, *Composite Materials: Science and Applications* (Springer Science & Business Media, 2010).

3. F. Meirer, B. M. Weckhuysen, Spatial and temporal exploration of heterogeneous catalysts with synchrotron radiation. *Nat. Rev. Mater.* **3**, 324–340 (2018).

4. V. Wood, X-ray tomography for battery research and development. *Nat. Rev. Mater.* **3**, 293–295 (2018).

5. D. Kim, M. Chung, J. Carnis, S. Kim, K. Yun, J. Kang, W. Cha, M. J. Cherukara, E. Maxey, R. Harder, K. Sasikumar, S. K. R. S. Sankaranarayanan, A. Zozulya, M. Sprung, D. Riu, H. Kim, Active site localization of methane oxidation on Pt nanocrystals. *Nat. Commun.* **9**, 3422 (2018).

6. T. Famprikis, P. Canepa, J. A. Dawson, M. S. Islam, C. Masquelier, Fundamentals of inorganic solid-state electrolytes for batteries. *Nat. Mater.* **18**, 1278–1291 (2019).

7. F. de Groot, High-resolution x-ray emission and x-ray absorption spectroscopy. *Chem. Rev.* **101**, 1779–1808 (2001).

8. J. A. van Bokhoven, C. Lamberti, in *Nanotechnology in Catalysis* (Wiley-VCH Verlag GmbH & Co. KGaA, 2017), pp. 1029–1054.

9. S. C. Garcea, Y. Wang, P. J. Withers, X-ray computed tomography of polymer composites. *Compos. Sci. Technol.* **156**, 305–319 (2018).

10. C. Y. J. Hémonnot, S. Köster, Imaging of biological materials and cells by x-ray scattering and diffraction. *ACS Nano* **11**, 8542–8559 (2017).

11. P. J. Withers, M. Preuss, Fatigue and damage in structural materials studied by x-ray tomography. *Annu. Rev. Mater. Res.* **42**, 81–103 (2012).

12. G. Schmid, M. Obst, J. Wu, A. Hitchcock, in *X-ray and Neutron Techniques for Nanomaterials Characterization*, C. S. S. R. Kumar, Ed. (Springer Berlin Heidelberg, 2016), pp. 43–94.

13. F. Meirer, J. Cabana, Y. Liu, A. Mehta, J. C. Andrews, P. Pianetta, Three-dimensional imaging of chemical phase transformations at the nanoscale with full-field transmission x-ray microscopy. *J. Synchrotron Rad.* **18**, 773–781 (2011).

14. M. Hirose, N. Ishiguro, K. Shimomura, D.-N. Nguyen, H. Matsui, H. C. Dam, M. Tada, Y. Takahashi, Oxygen-diffusion-driven oxidation behavior and tracking areas visualized by x-ray spectro-ptychography with unsupervised learning. *CommChem* **2**, 50 (2019).

15. J. Wang, Y.-c. K. Chen-Wiegart, C. Eng, Q. Shen, J. Wang, Visualization of anisotropic-isotropic phase transformation dynamics in battery electrode particles. *Nat. Commun.* **7**, 12372 (2016).

16. J. Ihli, D. F. Sanchez, R. R. Jacob, V. Cuartero, O. Mathon, F. Krumeich, C. Borca, T. Huthwelker, W.-C. Cheng, Y. Y. Shu, S. Pascarelli, D. Grolimund, A. Menzel, J. A. van Bokhoven, Localization and specification of iron impurities within a fluid catalytic cracking catalyst. *Angew. Chem. Int. Ed.* **56**, 14031–14035 (2017).

17. S. W. T. Price, K. Ignatyev, K. Geraki, M. Basham, J. Filik, N. T. Vo, P. T. Witte, A. M. Beale, J. F. W. Mosselmans, Chemical imaging of single catalyst particles with scanning μ-XANES-CT and μ-XRF-CT. *Phys. Chem. Chem. Phys.* **17**, 521–529 (2015).

18. J. Becher, D. F. Sanchez, D. E. Doronkin, D. Zengel, D. M. Meira, S. Pascarelli, J.-D. Grunwaldt, T. L. Sheppard, Chemical gradients in automotive Cu-SSZ-13 catalysts for NO_x removal revealed by operando x-ray spectrotomography. *Nat. Catal.* **4**, 46–53 (2021).

19. E. Maire, P. J. Withers, Quantitative x-ray tomography. *Int. Mater. Rev.* **59**, 1–43 (2014).

20. R. A. Crowther, D. J. DeRosier, A. Klug, The reconstruction of a three-dimensional structure from projections and its application to electron microscopy. *Proc. R. Soc. A* **317**, 319–340 (1970).

21. A. H. Andersen, A. C. Kak, Simultaneous algebraic reconstruction technique (SART): A superior implementation of the ART algorithm. *Ultrason. Imaging* **6**, 81–94 (1984).

22. M. Dierolf, A. Menzel, P. Thibault, P. Schneider, C. M. Kewish, R. Wepf, O. Bunk, F. Pfeiffer, Ptychographic x-ray computed tomography at the nanoscale. *Nature* **467**, 436–439 (2010).

23. M. Ruitenbeek, R. A. Overbeek, D. C. Koningsberger, J. W. Geus, in *Catalytic Activation and Functionalisation of Light Alkanes: Advances and Challenges*, E. G. Derouane, J. Haber, F. Lemos, F. R. Ribeiro, M. Guisnet, Eds. (Springer, 1998), pp. 423–427.

24. B. K. Hodnett, Vanadium-phosphorus oxide catalysts for the selective oxidation of C_4 hydrocarbons to maleic anhydride. *Catal. Rev.* **27**, 373–424 (1985).

25. M. Ruitenbeek, A. Barbon, E. E. van Faassen, J. W. Geus, Evidence for a new type of vanadyl pairs in $(VO)_2P_2O_7$: An ESR and magnetisation study. *Catal. Lett.* **54**, 101–104 (1998).

26. M. Ruitenbeek, thesis, Utrecht University, Utrecht (1999).

27. F. Benzi, G. Giuli, S. Della Longa, E. Paris, Vanadium *K*-edge XANES in vanadium-bearing model compounds: A full multiple scattering study. *J. Synchrotron Radiat.* **23**, 947–952 (2016).

28. G. J. Hutchings, Vanadium phosphate: A new look at the active components of catalysts for the oxidation of butane to maleic anhydride. *J. Mater. Chem.* **14**, 3385–3395 (2004).

29. J. Wong, F. W. Lytle, R. P. Messmer, D. H. Maylotte, *K*-edge absorption spectra of selected vanadium compounds. *Phys. Rev. B.* **30**, 5596–5610 (1984).

30. S. Böcklein, G. Mestl, S. V. Auras, J. Wintterlin, On the correlation of structure and catalytic performance of VPO catalysts. *Top. Catal.* **60**, 1682–1697 (2017).

31. N. F. Dummer, J. K. Bartley, G. J. Hutchings, in *Advances in Catalysis*, B. C. Gates, H. Knözinger, Eds. (Academic Press, 2011), vol. 54, pp. 189–247.

32. D. J. Thompson, M. O. Fanning, B. K. Hodnett, Modelling the active sites in vanadyl pyrophosphate. *J. Mol. Catal. A Chem.* **198**, 125–137 (2003).

33. M.-J. Cheng, W. A. Goddard III, R. Fu, The reduction-coupled oxo activation (ROA) mechanism responsible for the catalytic selective activation and functionalization of *n*-butane to maleic anhydride by vanadium phosphate oxide. *Top. Catal.* **57**, 1171–1187 (2014).

34. P. L. Gai, K. Kourtakis, Solid-state defect mechanism in vanadyl pyrophosphate catalysts: Implications for selective oxidation. *Science* **267**, 661–663 (1995).

35. G. Bergeret, M. David, J. P. Broyer, J. C. Volta, G. Hecquet, A contribution to the knowledge of the active sites of VPO catalysts for butane oxidation to maleic anhydride. *Catal. Today* **1**, 37–47 (1987).

36. A. Bortinger, G. Mazzoni, T. Monti, Phosphorus/vanadium catalyst preparation, U. S. patent number 6,858,561, U.S. Patent and Trademark Office (2005).

37. A. Kaestner, B. Münch, P. Trtik, L. Butler, Spatiotemporal computed tomography of dynamic processes. *Opt. Eng.* **50**, 123201–123209 (2011).

38. J. W. Gibbs, K. A. Mohan, E. B. Gulsoy, A. J. Shahani, X. Xiao, C. A. Bouman, M. De Graef, P. W. Voorhees, The three-dimensional morphology of growing dendrites. *Sci. Rep.* **5**, 11824 (2015).

39. K. Pearson, LIII. On lines and planes of closest fit to systems of points in space. *Philos. Mag.* **2**, 559–572 (1901).

40. B. Watts, Calculation of the Kramers-Kronig transform of x-ray spectra by a piecewise Laurent polynomial method. *Opt. Express* **22**, 23628–23639 (2014).

41. K. Ohta, H. Ishida, Comparison among several numerical integration methods for kramers-kronig transformation. *Appl. Spectrosc.* **42**, 952–957 (1988).

42. B. Ravel, M. Newville, ATHENA, ARTEMIS, HEPHAESTUS: Data analysis for x-ray absorption spectroscopy using IFEFFIT. *J. Synchrotron Radiat.* **12**, 537–541 (2005).

43. B. A. Palmer, G. R. Edwards-Gau, B. M. Kariuki, K. D. M. Harris, I. P. Dolbnya, S. P. Collins, x-ray birefringence imaging. *Science* **344**, 1013–1016 (2014).

44. P. T. Nguyen, R. D. Hoffman, A. W. Sleight, Structure of $(VO)_2P_2O_7$. *Mater. Res. Bull.* **30**, 1055–1063 (1995).

45. Z. Gao, M. Holler, M. Odstrcil, A. Menzel, M. Guizar-Sicairos, J. Ihli, Nanoscale crystal grain characterization via linear polarization x-ray ptychography. *Chem. Commun.* **56**, 13373–13376 (2020).

46. The circles of light. *Nat. Rev. Mater.* **3**, 281–282 (2018).

47. G. Vlaic, D. Andreatta, P. E. Colavita, Characterisation of heterogeneous catalysts by EXAFS. *Catal. Today* **41**, 261–275 (1998).

48. M. Holler, J. Ihli, E. H. R. Tsai, F. Nudelman, M. Verezhak, W. D. J. van de Berg, S. H. Shahmoradian, A lathe system for micrometre-sized cylindrical sample preparation at room and cryogenic temperatures. *J. Synchrotron Radiat.* **27**, 472–476 (2020).

49. S. Gorelick, J. Vila-Comamala, V. A. Guzenko, R. Barrett, M. Salomé, C. David, High-efficiency Fresnel zone plates for hard x-rays by 100 keV e-beam lithography and electroplating. *J. Synchrotron Radiat.* **18**, 442–446 (2011).

50. M. Odstrčil, M. Lebugle, M. Guizar-Sicairos, C. David, M. Holler, Towards optimized illumination for high-resolution ptychography. *Opt. Express* **27**, 14981–14997 (2019).

51. M. Holler, A. Diaz, M. Guizar-Sicairos, P. Karvinen, E. Färm, E. Härkönen, M. Ritala, A. Menzel, J. Raabe, O. Bunk, X-ray ptychographic computed tomography at 16 nm isotropic 3D resolution. *Sci. Rep.* **4**, 3857 (2014).

52. X. Huang, H. Yan, R. Harder, Y. Hwu, I. K. Robinson, Y. S. Chu, Optimization of overlap uniformness for ptychography. *Opt. Express* **22**, 12634–12644 (2014).

53. T. Kohler, A projection access scheme for iterative reconstruction based on the golden section, in *IEEE Symposium Conference Record Nuclear Science* (IEEE, 2004), vol. 6, pp. 3961–3965.

54. P. Thibault, M. Dierolf, A. Menzel, O. Bunk, C. David, F. Pfeiffer, High-resolution scanning x-ray diffraction microscopy. *Science* **321**, 379–382 (2008).

55. P. Thibault, M. Guizar-Sicairos, Maximum-likelihood refinement for coherent diffractive imaging. *New J. Phys.* **14**, 063004 (2012).

56. K. Wakonig, H.-C. Stadler, M. Odstrčil, E. H. R. Tsai, A. Diaz, M. Holler, I. Usov, J. Raabe, A. Menzel, M. Guizar-Sicairos, PtychoShelves, a versatile high-level framework for high-performance analysis of ptychographic data. *J. Appl. Cryst.* **53**, 574–586 (2020).

57. J. Ihli, A. Diaz, Y. Shu, M. Guizar-Sicairos, M. Holler, K. Wakonig, M. Odstrcil, T. Li, F. Krumeich, E. Müller, W.-C. Cheng, J. Anton van Bokhoven, A. Menzel, Resonant ptychographic tomography facilitates three-dimensional quantitative colocalization of catalyst components and chemical elements. *J. Phys. Chem. C* **122**, 22920–22929 (2018).

58. A. Averbuch, R. R. Coifman, D. L. Donoho, M. Elad, M. Israeli, Fast and accurate polar Fourier transform. *Appl. Comput. Harmon. Anal.* **21**, 145–167 (2006).

59. M. Odstrčil, M. Holler, J. Raabe, M. Guizar-Sicairos, Alignment methods for nanotomography with deep subpixel accuracy. *Opt. Express* **27**, 36637–36652 (2019).

60. G. T. Herman, *Fundamentals of Computerized Tomography: Image Reconstruction from Projections* (Springer Publishing Company Incorporated, 2009).

61. D. C. Koningsberger, R. Prins, *X-ray Absorption: Principles, Applications, Techniques of EXAFS, SEXAFS, and XANES* (John Wiley and Sons, 1988).

62. M. van Heel, M. Schatz, Fourier shell correlation threshold criteria. *J. Struct. Biol.* **151**, 250–262 (2005).

63. M. R. Howells, T. Beetz, H. N. Chapman, C. Cui, J. M. Holton, C. J. Jacobsen, J. Kirz, E. Lima, S. Marchesini, H. Miao, D. Sayre, D. A. Shapiro, J. C. H. Spence, D. Starodub, An assessment of the resolution limitation due to radiation-damage in x-ray diffraction microscopy. *J. Electron. Spectrosc. Relat. Phenom.* **170**, 4–12 (2009).

64. T. Hildebrand, P. Rüegsegger, A new method for the model-independent assessment of thickness in three-dimensional images. *J. Microsc.* **185**, 67–75 (1997).

65. L. Lutterotti, S. Matthies, H. Wenk, MAUD: A friendly Java program for material analysis using diffraction, IUCr: Newsletter of the CPD 21 (1999).

66. J. Trampert, J.-J. Leveque, Simultaneous iterative reconstruction technique: Physical interpretation based on the generalized least squares solution. *J. Geophys. Res. Solid Earth* **95**, 12553–12559 (1990).

67. J. Kieffer, D. Karkoulis, PyFAI, a versatile library for azimuthal regrouping. *J. Phys. Conf. Ser.* **425**, 202012 (2013).

68. P. Bleuet, E. Welcomme, E. Dooryhee, J. Susini, J.-L. Hodeau, P. Walter, Probing the structure of heterogeneous diluted materials by diffraction tomography. *Nat. Mater.* **7**, 468–472 (2008).

69. W. De Nolf, F. Vanmeert, K. Janssens, XRDUA: Crystalline phase distribution maps by two-dimensional scanning and tomographic (micro) x-ray powder diffraction. *J. Appl. Cryst.* **47**, 1107–1117 (2014).

70. J. Miao, T. Ishikawa, I. K. Robinson, M. M. Murnane, Beyond crystallography: Diffractive imaging using coherent x-ray light sources. *Science* **348**, 530–535 (2015).

71. Y.-S. Yu, M. Farmand, C. Kim, Y. Liu, C. P. Grey, F. C. Strobridge, T. Tyliszczak, R. Celestre, P. Denes, J. Joseph, H. Krishnan, F. R. N. C. Maia, A. L. D. Kilcoyne, S. Marchesini, T. P. C. Leite, T. Warwick, H. Padmore, J. Cabana, D. A. Shapiro, Three-dimensional localization of nanoscale battery reactions using soft x-ray tomography. *Nat. Commun.* **9**, 921 (2018).

72. V. Blum, R. Gehrke, F. Hanke, P. Havu, V. Havu, X. Ren, K. Reuter, M. Scheffler, Ab initio molecular simulations with numeric atom-centered orbitals. *Comput. Phys. Commun.* **180**, 2175–2196 (2009).

73. X. Ren, P. Rinke, V. Blum, J. Wieferink, A. Tkatchenko, A. Sanfilippo, K. Reuter, M. Scheffler, Resolution-of-identity approach to Hartree-Fock, hybrid density functionals, RPA, MP2 and *GW* with numeric atom-centered orbital basis functions. *New J. Phys.* **14**, 053020 (2012).

74. J. P. Perdew, K. Burke, M. Ernzerhof, Generalized gradient approximation made simple. *Phys. Rev. Lett.* **77**, 3865–3868 (1996).

75. S. N. Achary, S. J. Patwe, A. K. Tyagi, Crystal structure and thermal expansion studies of α-$VO(PO_3)_2$. *J. Alloys Compd.* **461**, 474–480 (2008).

76. F. K. Hannour, A. Martin, B. Kubias, B. Lücke, E. Bordes, P. Courtine, Vanadium phosphorus oxides with P/V=2 used as oxidation and ammoxidation catalysts. *Catal. Today* **40**, 263–272 (1998).

77. J. W. Johnson, D. C. Johnston, A. J. Jacobson, J. F. Brody, Preparation and characterization of vanadyl hydrogen phosphate hemihydrate and its topotactic transformation to vanadyl pyrophosphate. *J. Am. Chem. Soc.* **106**, 8123–8128 (1984).

78. M. E. Leonowicz, J. W. Johnson, J. F. Brody, H. F. Shannon, J. M. Newsam, Vanadyl hydrogenphosphate hydrates: $VO(HPO_4)\cdot 4H_2O$ and VO(HPO4)·0.5H_2O. *J. Solid State Chem.* **56**, 370–378 (1985).

79. H. R. Tietze, The crystal and molecular structure of oxovanadium(V) orthophosphate dihydrate, $VOPO_4$,2H_2O. *Aust. J. Chem.* **34**, 2035–2038 (1981).